RESEARCH ARTICLE

Selective efficient photocatalytic degradation of antibiotics and direct Z-type migration pathway for hierarchical core–shell TiO$_2$/g-C$_3$N$_4$ composites

Hu Liu[1] · Jianmei Pan[1] · Keyu E[1] · Yi Guan[1] · Wenbo Gou[1] · Peng Wang[1] · Shahid Hussain[1] · Ze Du[1] · Chengfei Ma[1]

Abstract

Constructing superior Z-type photocatalytic heterojunction is beneficial to effectively enlarge interface contact, improve the photo-generated carrier separation rate, and retain the high redox ability. In this work, we designed a hierarchical core–shell g-C$_3$N$_4$/TiO$_2$ structure to build Z-type heterojunction via combining simple template method and pyrolysis process. A close-knit Z-type heterojunction was constructed using TiO$_2$ as a thick core and g-C$_3$N$_4$ as an ultra-thin shell. The effects of lamp source, wavelength, tetracycline (TC) concentration, and photocatalyst dose on the degradation performance on TC of g-C$_3$N$_4$/TiO$_2$ were inspected. 0.1TiO$_2$/g-C$_3$N$_4$ photocatalyst had the best degradation rate and highest removal rate within 30 min, and its degradation rate was about 49, 23, and 5 times than pure g-C$_3$N$_4$, TiO$_2$, and commercial TiO$_2$/g-C$_3$N$_4$ in respect. Moreover, compared with degradation ability under Xenon lamp, LED irradiation for g-C$_3$N$_4$/TiO$_2$ composites showed a remarkable selective degradation. The fast and efficient Z-type transfer pathway of 0.1 g-C$_3$N$_4$/TiO$_2$ was realized by forming an optimized interface and abundant surface active sites ascribed to the combined action of thick TiO$_2$ core and ultra-thin g-C$_3$N$_4$ shell. In addition, the degradation intermediates were analyzed by LC–MS and suggested pathways of degradation. The work could provide novel design concept to obtain reliable Z-type photocatalysts with hierarchical core–shell structure applied in degradation of antibiotic wastewater.

Keywords Z-type heterojunction · Core–shell · g-C$_3$N$_4$ · Photocatalyst · Tetracycline

Introduction

Antibiotics as a great discovery in human history has been widely used in many fields, such as medical, animal husbandry, and aquaculture (Kayal and Mandal 2022). However, the produced antibiotic wastewater causes the environmental pollution and seriously endangers the health and safety of human and other organisms. It is untoward to deal with antibiotic wastewater efficiently due to its complicated composition, biological toxicity, non-biodegradability, and high concentration. Thus, it is

imperative to develop efficient and simple antibiotic treatment techniques. Among many strategies, photocatalytic technology has attracted plenty of attention due to its superiorities of good reliability, high degradation efficiency, and outstanding cyclicity. Photocatalysis, as a promising advanced oxidation process (AOP) (Dewil et al. 2017; Milh et al. 2021), can generate highly oxidizing free radicals and other strong oxidizers in the water via light irradiation, which can efficiently degrade recalcitrant pollutants into innoxious substances. It is well known that titanium oxide (TiO$_2$) is one of the preferred photocatalysts for the commercial application, thanks to its durable physical and chemical stability, good photo-corrosion resistance, abundant natural resource, high photocatalytic efficiency, non-toxicity, and low cost (Meng et al. 2019), which shows the extensive applications, such as wastewater treatment water splitting, sterilization, and carbon dioxide reduction. Generally, there mainly exist three crystal structures of TiO$_2$: anatase, rutile, and brookite. The anatase TiO$_2$ commonly has the better photocatalytic activity compared with other

forms of TiO_2 due to the super hydrophilicity, large band gap, and high surface area. However, it still suffers several defects, such as low light utilization, low quantum efficiency, and rapid recombination between electrons (e^-) and holes (h^+), thus greatly limiting its photocatalytic activity. At present, many methods including morphological control (Jo and Natarajan 2015), element doping (Kong et al. 2018), dye sensitization (Hao et al. 2018), and heterojunction structure (Maziarz 2019) are widely used to improve the photocatalytic performance. In particular, the construction of direct Z-type heterojunction has been a research hotspot due to the significant advantages of this system. The system can complete the oxidation reaction on a photocatalyst with more positive valence band and reduction reaction on a photocatalyst with more negative conduction band, which can effectively accelerate the separation and migration rate of photo-generated e^- and h^+ and retain the high redox performance. Furthermore, it also can extend the light absorption range, reduce the unfavorable reactions, and enhance the stability of direct Z-type heterojunction (Chen et al. 2022). Hao et al. (2017) prepared rutile TiO_2/graphite carbon nitride (TiO_2/g-C_3N_4) core–shell nanorods using a saturated aqueous solution route, which presented higher photocatalytic degradation performance of Rhodamine B in contrast with pure TiO_2 and pure g-C_3N_4 under visible-light on account of the superb separation efficiency of photo-generated carriers by a Z-scheme heterojunction. Zuo et al. (2021) fabricated a Z-scheme TiO_2/$ZnIn_2S_4$ nanoflower heterojunction from ultrathin TiO_2 nanosheets integrated into $ZnIn_2S_4$, showing an enhanced photocatalytic H_2 and O_2 evolution activities and wonderful stability without sacrificial agent due to the higher redox potentials and prohibition of carrier recombination in system. Yu et al. (2013) synthesized a direct g-C_3N_4/TiO_2 Z-type photocatalyst via an easy calcination method using P25 TiO_2 (30 nm) and urea as the raw materials. The intimate heterojunctions were composed of P25 nanoparticles enfolded by ultrathin g-C_3N_4 sheets, which could enable the fast transport of carriers at the interface to obtain the improved decomposition performance of formaldehyde (HCHO). Therefore, it was essential to optimize the direct Z-scheme migration route via constructing suitable nano-heterojunction structure. As a non-metallic photocatalyst, g-C_3N_4 could be applied in the degradation, hydrogen production, and reduction of carbon dioxide for superiorities of high specific surface area, stable properties, and low cost (Pan et al. 2022, 2023;). It was reported that Z-type g-C_3N_4/TiO_2 heterojunctions for advanced oxidation were developed via numbers of methods such as wetness impregnation, defect-assisted modification, saturated aqueous solution method, and solvothermal method. However, there were few reports on using template method to construct a hierarchical core–shell structure to establish

Z-type g-C_3N_4/TiO_2 heterojunction. Furthermore, although Z-type g-C_3N_4/TiO_2 presented extended photocatalytic activity and stability via different methods, it was still a great challenging to construct optimal Z-type g-C_3N_4/TiO_2 heterojunction to obtain the reliable interface for rapid divorce and transfer of carriers (Rehman et al. 2022).

Herein, we designed a hierarchical core–shell g-C_3N_4/TiO_2 structure via combining of a simple template method and pyrolysis process. The tight Z-scheme heterojunction was built from TiO_2 as a thick core and g-C_3N_4 as an ultrathin shell, which could vastly shorten the transfer distance and enhanced the movement and division efficiency of photogenerated carriers. The effects at different conditions (such as light source, wavelength band, dose, and TiO_2 amount) on the photocatalytic degradation performances of antibiotic were measured in detailed. The composite showed the selective efficient degradation ability under LED light irradiation. The g-C_3N_4/TiO_2 sample presented enhanced degradation ability of antibiotic due to their coupling effect from special interface and Z-scheme pathway in contrast to pure g-C_3N_4 and TiO_2.

Experimental part

Preparation of porous TiO_2 nanomaterials

First, 0.12 g of silica (SiO_2) nanopowders were dissolved in 80 ml of ethanol; then, 0.5 ml ammonium hydroxide was added and the blend was mixed evenly by stirring for 60 min at indoor temperature. Then, 1.2 ml of tetrabutyl titanate (TBT) was put into solution, and the reaction was stirred continuously at 50 °C for 16 h. The reaction was washed with deionized water and absolute ethanol, and dried in vacuo at 60 °C for 10 h. Subsequently, the products were kept at 550 °C in air for 2 h, and the heating rate was 5 °C/min to prepare SiO_2@TiO_2 composites. The composites were treated with 5% hydrogen fluoride solution to remove the SiO_2 template. Ultimately, the porous anatase TiO_2 nanomaterials were prepared by cleaning with deionized water and absolute ethanol. Then, the products were dried under vacuum at 60 °C for 10 h.

Preparation of direct Z-type g-C_3N_4/TiO_2 composites

The flow chart for preparing direct Z-type TiO_2/g-C_3N_4 composites was shown in Fig. S1. First, porous TiO_2 (0.05 g, 0.1 g, and 0.15 g) and thiourea (2 g) were added into ethanol and blended for 1 h. Subsequently, the obtained product was then dried and kept at 550 °C for 2 h, and temperature rate was 5 °C/min. After cooling, the $x$$TiO_2$/g-$C_3N_4$ composites were obtained, which were recorded as 0.05TiO_2/g-C_3N_4, 0.1TiO_2/g-C_3N_4 and 0.15TiO_2/g-C_3N_4, respectively. Pure

g-C$_3$N$_4$ was prepared by holding thiourea at 550 °C for 2 h at a temperature rate of 5 °C/min. For comparison, the commercial TiO$_2$ (0.1 g) was also used for preparing commercial TiO$_2$/g-C$_3$N$_4$ at the same experimental conditions.

Material characterization

The XRD diffraction pattern of the sample was determined by D8 ADVANCE diffractometer (Cu Kα diffraction source) test result (test range was $2\theta = 10 \sim 80°$, scanning speed was 5° min^{-1}). The Fourier transform infrared (FTIR) spectra of each sample were measured with Nicolet Nexus 470 infrared spectrometer (test range was 400–4000 cm^{-1}, with KBr as substrate). Scanning electron microscope (SEM, JSM-7800F) and transmission electron microscope(TEM, FEI Talos 200S) were used to analyze the morphology characteristics and element distribution of each sample. X-ray photoelectron spectroscopy (XPS) of each sample was obtained by X-ray photoelectron spectrometer (Thermo Scientific K-Alpha). Ultraviolet–visible (UV–Vis) reflectance spectra of all samples were obtained by spectrophotometer (UV2600) (test wavelength range was 300–400 nm, and high-purity BaSO$_4$ was used as reference). The Steady-state PL spectra of the samples were tested by QuantaMaster™-40 with an excitation wavelength of 365 nm.

Photocatalytic degradation experiment

The photocatalytic activity of all specimens were estimated by photocatalytic degradation of TC. First, 50 ml TC water solution was diffused with10 mg photocatalyst. After dark reaction in 30 min, the equilibrium of adsorption–desorption was reached; then, experimental light source was turned on. An 80 W LED lamp ($\lambda = 365$ nm, 420 nm, 850 nm) and a 300-W Xe lamp ($\lambda = 200$–400 nm) were selected as the experimental light sources, and the distance between the lamp cap and the reaction vessel was about 10 cm. The reaction beaker was placed on the magnetic agitator to ensure that the reaction solution was in a stable state of continuous agitation, and then, the agitator and light source were turned on to conduct the photocatalytic degradation experiment. By gathering a certain amount of reaction solution at different times (0, 1, 3, 5, 15, 30 min) and filtered by 0.22 μm filter head to determine TC concentration (measured at 300–400 nm by ultraviolet spectrophotometer).

Photoeletric chemical test

The CHI 660E electrochemical workstation (three electrode system) was used for photochemical tests. The preparation process of the working electrode was as followed: 5 mg samples were added into a 5-ml centrifuge tube, then 40 μL

membrane solution, 250 μL glycol, and 250 μL anhydrous ethanol were added, and then, ultrasonic was performed for 30 min to gain a uniform suspension. Then, the suspension (80 μL) was evenly covered on FTO conductive glass with a pipette gun, and was placed at 80 °C for 6 h until dry. The electrolyte was Na$_2$SO$_4$ aqueous solution (0.5 mol/L). The counter electrode was platinum electrode, and reference electrode was Ag/AgCl. The photocurrent, electrochemical impedance, and Schottky characteristics of the materials were tested by using this workstation.

Results and discussion

XRD and FTIR analysis

Figure 1a shows the XRD patterns of TiO$_2$, g-C$_3$N$_4$, and xTiO$_2$/g-C$_3$N$_4$ samples. And there existed two characteristic diffraction peaks in pure g-C$_3$N$_4$, located at 13.1° and 28.1°° corresponding to (100) crystal plane of in-plane structural stacking in g-C$_3$N$_4$ and the (002) crystal plane caused by interlayer stacking of conjugated aromatic hydrocarbons (JCPDS No.87–1526) (Li et al. 2017). There were obvious diffraction peaks at 25.5°, 37.6°, 48.1°, 53.9°, 55.0°, 62.7°, and 68.8°, corresponding to crystal planes of (101), (004), (200), (105), (211), (204), and (116) in TiO$_2$ samples, respectively, indicating that only anatase phase TiO$_2$ existed (JCPDS No.21–1272) (Li et al. 2022). For xTiO$_2$/g-C$_3$N$_4$ sample, there existed obvious diffraction peaks of TiO$_2$. However, it is difficult to observe the characteristic peak of g-C$_3$N$_4$ in xTiO$_2$/g-C$_3$N$_4$ owing to poor content of g-C$_3$N$_4$ obtained from thiourea after pyrolysis. Furthermore, with raising TiO$_2$ amount, the peak intensity and position of xTiO$_2$/g-C$_3$N$_4$ composites had no evident change, indicating that the addition of TiO$_2$ had little influence on the phase composition.

Figure 1b shows the chemical compositions of the samples and FTIR spectra were used for analysis. For single TiO$_2$ and xTiO$_2$/g-C$_3$N$_4$ samples, the absorption peak at 400–800 cm^{-1} was caused by the stretching vibration of Ti–O-Ti. And 1600 cm^{-1} and 3350 cm^{-1} were absorption peaks caused by the adsorption of H$_2$O and surface O–H vibration (Monga and Basu 2019). The sharp absorption peak of pure g-C$_3$N$_4$ at 808 cm^{-1} was mainly due to out-of-plane bending vibration of triazine unit. The forceful and broad absorption band between 1200 and 1700 cm^{-1} was mainly attributed to the stretching vibration in C-N and C=N of typical S-triazine ring. The broad absorption peaks in the range of 3450–3150 cm^{-1} were assigned to the tensile vibration of N–H or O–H (Jiang et al. 2018a, b). Compared with single g-C$_3$N$_4$, recognize typical characteristic peak of g-C$_3$N$_4$ in xTiO$_2$/g-C$_3$N$_4$ was tough, mainly thanks to low percentage of g-C$_3$N$_4$ in composite. Besides, xTiO$_2$/g-C$_3$N$_4$

Fig. 1 **a** XRD patterns; **b** FTIR spectra of TiO_2, g-C_3N_4, and xTiO$_2$/g-C_3N_4 composites; high resolution spectra of TiO_2, g-C_3N_4, and xTiO$_2$/g-C_3N_4 composites **c** C 1s, **d** N 1s, **e** Ti 2p, and **f** O 1s

retained the characteristic absorption peak of TiO_2. With raising TiO_2 content, the intensity of the stretching vibration peak of Ti–O-Ti was significantly enhanced. However, the position of Ti–O-Ti peak was not changed, suggesting that

the addition of g-C_3N_4 could be incapable of changing the chemical structure of the composites and could effectively build a heterojunction, which was conductive to the rapid transfer of carriers at the interface.

XPS analysis

To explore electronic chemical states of TiO_2, g-C_3N_4, and xTiO_2/g-C_3N_4, XPS analysis was conducted. Figure S2 presents the full XPS spectra of the samples that elements of C, N, O, and Ti were in composite simultaneously. Figure 1c is a high-resolution C 1 s spectrum with two peaks located at 284.8 eV and 288.3 eV, corresponding to sp^2 hybridized C in N–C = N and sp^2 C–C bond, respectively (Jiang et al. 2018a, b). The 286.4 eV was the peak which was corresponded to sp^2 C of aromatic ring on heptazine unit. In Fig. 1d, the N 1 s spectrum of pure g-C_3N_4 had three peaks at 398.6 eV, 400.1 eV, and 401.2 eV in consistent with the -NH_2 functional group, N-$(C)_3$, and sp^2 hybrid N(C-N = C), respectively. The high-resolution spectrum of O 1 s was presented in Fig. 1f. And peaks in pure TiO_2 at 529.2 eV and 531.2 eV were related to Ti–O bond and O–H bond adsorbed on the surface, respectively (Qiu et al. 2018). The Ti 2p spectrum of pure TiO_2 in Fig. 1e presented a binding energy of 456.9 eV in accordance with the split peak Ti $2p_{3/2}$ and the other binding energy at 463.6 eV corresponded to the split peak of Ti $2p_{1/2}$. It could be found that compared with pure g-C_3N_4, these binding energies of 0.1TiO_2/g-C_3N_4 had an apparent negative shift. Conversely, the binding energy at different positions for 0.1TiO_2/g-C_3N_4 appeared an evident positive shift than that of TiO_2, implying the viable electron move path from TiO_2 to g-C_3N_4.

SEM analysis

Figure 2 presents the figures of SEM and element mapping of xTiO_2/g-C_3N_4 so as to investigate the micromorphology, element composition, and distribution of the composites. Figure 2a–b show the SEM of 0.05TiO_2/g-C_3N_4 sample. It could be seen from the figure that the composite material was mainly composed of nanospheres and nanoparticles. Many nanoparticles and pores were found on the surface of the nanosphere in the corresponding enlarged image, indicating that the sample had a good hierarchical and porous structure and the surface of the hierarchical structure was flat. Pure TiO_2 appeared as relatively smooth nanospheres in Fig. S3. Once TiO_2 was covered with g-C_3N_4 nanoparticles, the active sites on the surface of composite increased, which promoted the rapid transfer of photogenerated charge carriers. With increasing TiO_2 amount, no apparent changes of the morphology for 0.1TiO_2/g-C_3N_4 were observed from the SEM images in both low and high magnification (Fig. 2c and d). With further raising TiO_2 amount, the particle sizes of 0.15TiO_2/g-C_3N_4 (Fig. 2e and f) increased significantly due to the accumulation of higher TiO_2 content, implying that the TiO_2 amount had a great impact on the microstructure of the composites. In addition, it could be seen that C, N, O, and Ti elements coexisted from EDS element mapping

of 0.1TiO_2/g-C_3N_4, and their distribution was uniform. And no Si element could be found, illustrating the completely etching of SiO_2 as the porous template. It was summed that g-C_3N_4 could cover on the exterior of TiO_2 to achieve a close heterojunction, which could enhance the separation and migration rates of carriers.

TEM analysis

Figure 2h shows the TEM images of 0.1 g-C_3N_4/TiO_2. It could be noted that the nanospheres were consist of many nanoparticles with uniform sizes, leading to the formation of obvious pores, which was in keeping with results of SEM. The corresponding TEM image proved nanoparticles from hierarchical structure with sizes of 10 ~ 20 nm were well distributed further which was presented in Fig. 2i. The corresponding HRTEM image in Fig. 2j further testified that the lattice distance of the sample was about 0.357 nm, which was in great accordance with the (101) crystal plane of anatase TiO_2. Furthermore, the TiO_2 surface was covered with ultrathin g-C_3N_4 sheets, suggesting a thick core-thin shell structure of the composite to form suitable heterojunctions, which was conducive to improve the carrier separation rate to obtain high photocatalytic efficiency.

Photocatalytic degradation performances

The antibiotic tetracycline (TC) was used as the degradation pollutant, and the initial concentration of its solution was 60 mg/L during the whole degradation processes. Figure S4 shows the photocatalytic performances of 0.1TiO_2/g-C_3N_4 under different degradation conditions. First, the pollutant concentration basically had no change under dark adsorption condition after 30 min, indicating that the adsorption reached the equilibrium. Subsequently, TC was degraded using irradiation of light at different wavelengths which was presented in Fig. S4(a), (d), and (g). It was found that the sample had the highest degradation rate of TC in 30 min under 365 nm attributed to the super light absorption ability under this wavelength, which could produce more photogenic charge carriers (Xu et al. 2020; Perumal et al. 2023). Meanwhile, it was easy to see that the degradation curves of 0.1TiO_2/g-C_3N_4 under 365@420 nm and 365 nm were similar, showing that the addition of visible light hardly enhanced the degradation effect of the samples. Besides, it was worth noting that 0.1TiO_2/g-C_3N_4 processed a moderate photocatalytic degradation rate under 200–400 nm, revealing that the sample had a good photocatalytic ability under ultraviolet B and C (UVB and UVC) due to the satisfying light absorption capacity. Also, the sample showed no photocatalytic effect under the near-infrared light of 850 nm attributed to the negligible light absorption level at this wavelength. The photocatalytic degradation kinetic
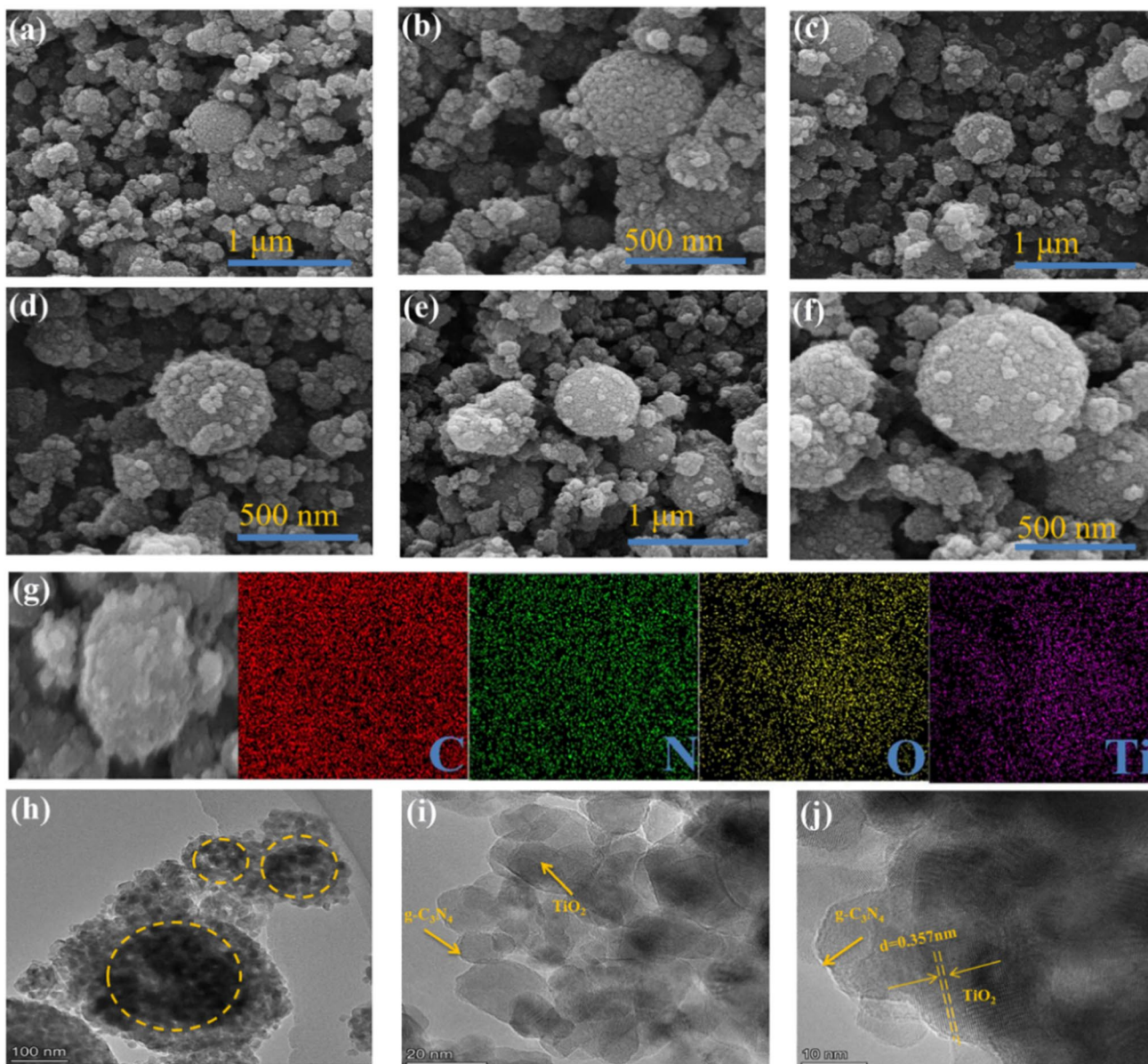
Fig. 2 SEM images of different xTiO$_2$/g-C$_3$N$_4$ composites **a–b** 0.05TiO$_2$/g-C$_3$N$_4$, **c–d** 0.1TiO$_2$/g-C$_3$N$_4$, **e–f** 0.15TiO$_2$/g-C$_3$N$_4$ and **g** 0.1TiO$_2$/g-C$_3$N$_4$ element map, **h** TEM images, and **i**, **j** high-magnification TEM images of TiO$_2$/g-C$_3$N$_4$ composites

curves of 0.1TiO$_2$/g-C$_3$N$_4$ sample were fitted by the following formula:

$$-\ln\left(\frac{C}{C_0}\right) = Kt \qquad (3.1)$$

C (mg/L) was the density of TC in solution in that moment, C_0 (mg/L) was the initial concentration of TC, and K (min^{-1}) was the rate constant of reaction (Liu et al. 2019; Yu et al. 2020). The obtained information was completely conformed to the quasi first-order kinetic equation after linear fitting. The K values at various wavelengths

(200~400 nm, 365 nm, 420 nm, 850 nm, and 365@420 nm) were 0.030, 0.049, 0.014, 0.000421, and 0.042, respectively, further inferring the efficient degradation of the sample at ultraviolet and visible regions.

Figure S4(c) shows the degradation efficiency of 0.1TiO$_2$/g-C$_3$N$_4$ photocatalyst (10 mg) at different concentrations of TC under 365 nm. The results showed the degradation ability gradually declined with growing TC concentration. The degradation kinetic curves of 0.1TiO$_2$/g-C$_3$N$_4$ were accord with the first-order kinetic equation which were presented in Fig. S4(f). The corresponding K values of TC in Fig. S4(i) at different concentrations were 0.076, 0.074, 0.054, and

0.049, respectively, showing a decreasing degradation rate with raising TC concentration. Generally, under the same degradation conditions, the catalyst had a fixed number of active groups and electron–hole pairs. When TC concentration was low, the active free radicals of the sample were sufficient to degrade pollutant effectively. However, when TC concentration reached a higher concentration, the sample showed insufficient number of active free radicals leading to the weakness of photocatalysis and obvious decline of degradation rate. Figure S4(b, e, h) show the degradation performances of $0.1\mathrm{TiO_2}/\mathrm{g\text{-}C_3N_4}$ using various photocatalyst doses under 365 nm. Under the same test conditions, the degradation efficiency was positively correlated with photocatalyst amount. With increasing photocatalyst doses, the degradation efficiency was significantly enhanced. The pollutant could be completely removed after 30 min when adding a highest dose (15 mg), corresponding to a maximum degradation rate constant (0.076) and the best degradation ability because the high dose of photocatalyst provided more surface active sites and photo-generated carriers, which could effectively improve the photocatalytic degradation efficiency (Zhang et al. 2022).

Figure 3a shows the degradation performance of different samples under 365 nm using 10 mg photocatalyst. Among these samples, the degradation ability of prepared $x\mathrm{TiO_2}/\mathrm{g\text{-}C_3N_4}$ composites by template method was superior to that of commercial $\mathrm{TiO_2}/\mathrm{g\text{-}C_3N_4}$ due to more active sites for photogenic carrier transfer. Moreover, it could be found that after the dark adsorption reached the equilibrium, the value of C/C_0 for $0.1\mathrm{TiO_2}/\mathrm{g\text{-}C_3N_4}$ showed a more significant decrease with the extension of time compared with other samples, showing its highest degradation performance. From the fitted degradation kinetics curves (Fig. 3c), the degradation capability of $x\mathrm{TiO_2}/\mathrm{g\text{-}C_3N_4}$ was superior to single $\mathrm{g\text{-}C_3N_4}$. Besides, degradation efficiency was first enhanced and then weakened sharply with raising $\mathrm{TiO_2}$ amount. The increase of particle size of the composite and the decrease of the surface active sites after adding excessive $\mathrm{TiO_2}$ were not favoring to rapid migration of photogenerated carriers. Figure 3e shows the degradation kinetic rates of different samples. It could be clearly inferred that the $0.1\mathrm{TiO_2}/\mathrm{g\text{-}C_3N_4}$ composite presented the fastest degradation rate ($K=0.049$), which were about 49, 23, 4, 9, and 5 times to single $\mathrm{g\text{-}C_3N_4}$, $\mathrm{TiO_2}$, $0.05\mathrm{TiO_2}/\mathrm{g\text{-}C_3N_4}$, $0.15\mathrm{TiO_2}/\mathrm{g\text{-}C_3N_4}$, and commercial $\mathrm{TiO_2}/\mathrm{g\text{-}C_3N_4}$, respectively. It was confirmed that the appropriate heterojunction interface and good hierarchical structure of $0.1\mathrm{TiO_2}/\mathrm{g\text{-}C_3N_4}$ were conducive to the efficient separation and transfer of carries, which was compatible with the SEM analysis results (Hunge et al. 2021; Tang et al. 2021).

The degradation performance of different samples (10 mg) under the irradiation of 200–400 nm was seen in Fig. 3b, d, f. It was interesting to note that the prepared $x\mathrm{TiO_2}/\mathrm{g\text{-}C_3N_4}$ composites showed similarities in degradation

performance and the K values kept in the range of 0.021 to 0.030, suggesting that the additive amount of $\mathrm{TiO_2}$ had lesser effect on the photocatalytic performance of these composites using Xenon irradiation under ultraviolet light. Unlike Xenon irradiation at 200–400 nm, the ability of photocatalysis existed considerable difference in $x\mathrm{TiO_2}/\mathrm{g\text{-}C_3N_4}$ composites and K values remained in 0.006 to 0.049, implying that LED irradiation under 365 nm had remarkable selective degradation for various composites. It also could be seen that $0.1\mathrm{TiO_2}/\mathrm{g\text{-}C_3N_4}$ composite among all samples had the best photocatalytic efficiency under both two light irradiations in respect due to the suitable hierarchical structure and coated heterojunction. And the removal rate (R) and K value of TC was lower at 200–400 nm ($R=83\%$, $K=0.030$) than at 365 nm ($R=95\%$, $K=0.049$) because the sample produced fewer photogenerated carriers under 200–400 nm, which resulted a weaker degradation performance.

Photocatalytic degradation mechanism

UV − vis diffuse reflection spectroscopy was used to test the absorbance and forbidden band width (E_g) of samples in Fig. 4. Figure 4a shows the absorption edges of single $\mathrm{TiO_2}$ and $\mathrm{g\text{-}C_3N_4}$ were about 370 nm and 467 nm, respectively (Zong et al. 2019). The positions of absorption edge for $x\mathrm{TiO_2}/\mathrm{g\text{-}C_3N_4}$ and $0.15\mathrm{TiO_2}/\mathrm{g\text{-}C_3N_4}$ were essentially consistent with pure $\mathrm{TiO_2}$, indicating that $\mathrm{TiO_2}$ amount had little influence on the absorption edge of the composites. And $0.1\mathrm{TiO_2}/\mathrm{g\text{-}C_3N_4}$ displayed higher absorbance under ultraviolet and visible regions in contrast with pure $\mathrm{TiO_2}$ due to the construction of appropriate core–shell structure, leading an effective enhancement in degradation property under 365 nm and 420 nm. Figure 4b presents the calculated curves which indicated the E_g of single $\mathrm{TiO_2}$, $\mathrm{g\text{-}C_3N_4}$ were 3.17 and 2.38 eV, respectively. It was found that E_g of $x\mathrm{TiO_2}/\mathrm{g\text{-}C_3N_4}$ was superior to single $\mathrm{g\text{-}C_3N_4}$, showing stronger redox ability.

The Mott Schottky (M-S) curves obtained from various frequencies were presented in Fig. 4c, d. It was clearly seen that the slopes of samples of M-S curves of at different frequencies were positive, revealing the materials had n-type semiconductor characteristic. The conduction band potential (E_{CB}) of $\mathrm{g\text{-}C_3N_4}$ and $\mathrm{TiO_2}$ could be gained from $M\text{-}S$ curves. The intercept with the x-axis of $M\text{-}S$ curves was the flat-band potential (E_{fb} (Ag/AgCl)) of $\mathrm{TiO_2}$ and $\mathrm{g\text{-}C_3N_4}$, which were -0.58 V and -0.93 V, respectively. In conformity with the formula E_{fb} (NHE) $= E_{fb}$ (Ag/AgCl) $+ E_\theta$ (Ag/AgCl) $+ 0.059$ pH (pH $= 6.8$, E_θ (Ag/AgCl) $= 0.197$ eV), the conduction band potential (E_{CB}) was generally 0.3 V lower than that of E_{fB} (NHE). Thus, the E_{CB} values of $\mathrm{TiO_2}$, $\mathrm{g\text{-}C_3N_4}$ were -0.28 and -0.63 V (vs NHE). From the above result, the band gaps (E_g) of single $\mathrm{TiO_2}$, $\mathrm{g\text{-}C_3N_4}$ were 2.91 and 2.38 eV, respectively. The valence band potentials (E_{VB})
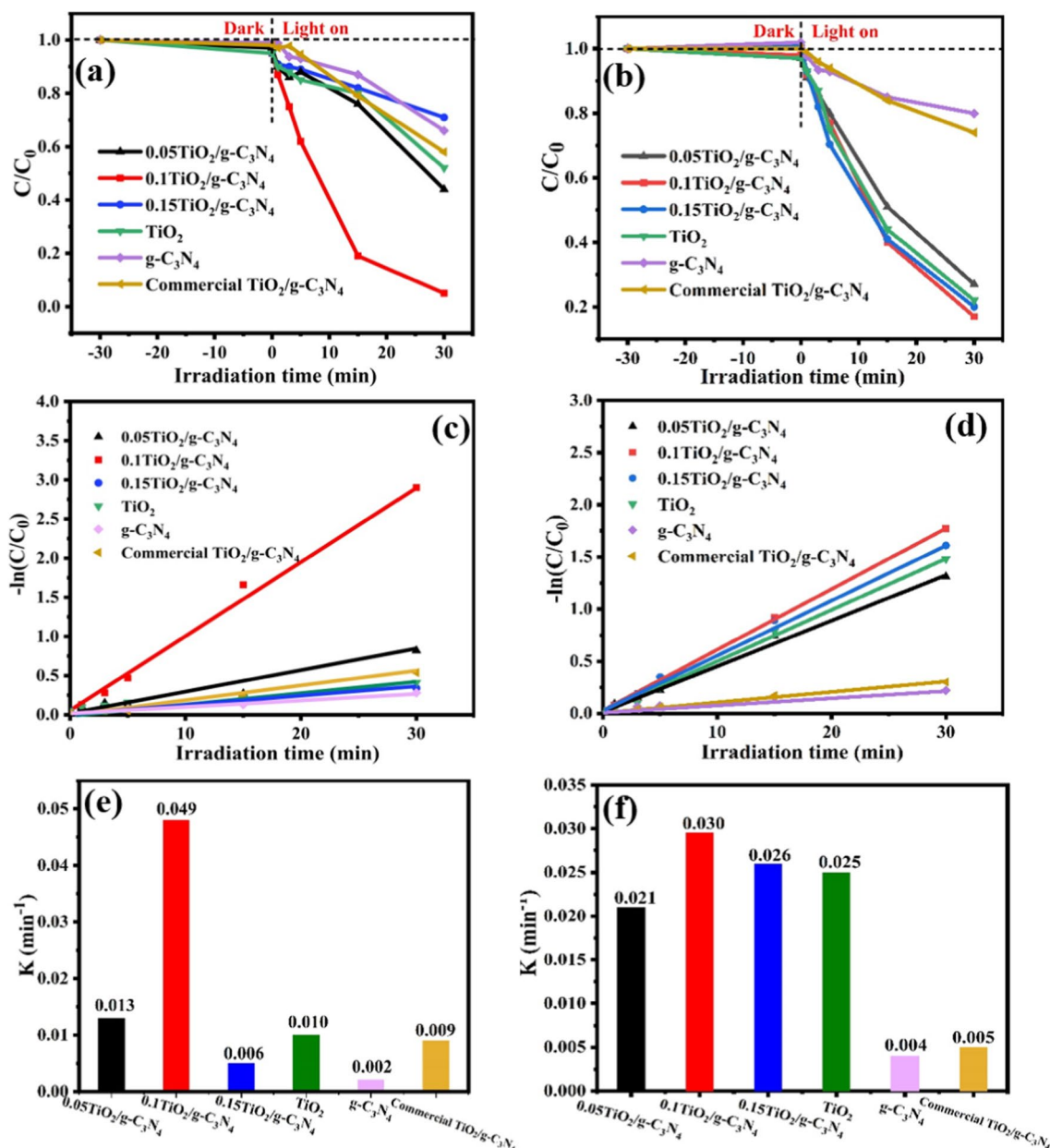
Fig. 3 Photocatalytic degradation performance of the samples: **a, b** C/C_0, **c, d** degradation kinetics curves, and **e, f** degradation rate constants under irradiations of 365 nm and 200–400 nm

were corresponded to 2.63 and 1.72 V (vs NHE) by combining with $E_{VB} = E_{CB} + E_g$.

The recombination and migration process of carriers for different samples were measured by PL spectroscopy in Fig. 5a. The PL intensity of single g-C_3N_4 was the best attribute to the rapid recombination of carriers. On contrary, the porous TiO_2 had awfully low intensity, inferring a fast separation and migration rate of carriers. Also, it could be observed that xTiO$_2$/g-C_3N_4 had extremely low PL strength due to their ideal heterostructures. The result clarified that the core–shell structure of the composites could effectively

promote the carrier transfer rate and restrain the recombination of carriers. With increasing TiO_2 amount, the PL strength had almost negligible change. It could be concluded that TiO_2 amount has a tiny impact on the PL strength of xTiO$_2$/g-C_3N_4, showing that the carries of the composites were easy to be separated.

EIS and transient photocurrent response of the samples were further carried out to analyze the transfer and divorce efficiencies of carriers (Fan et al. 2016). From Fig. 5c, it was shown that the photocurrent intensities of 0.5TiO$_2$/g-C_3N_4 and 0.1TiO$_2$/g-C_3N_4 were both significantly superior

Fig. 4 **a** UV–Vis curves and **b** band gaps of different samples. Mott Schottky curves of **c** TiO$_2$ and **d** g-C$_3$N$_4$
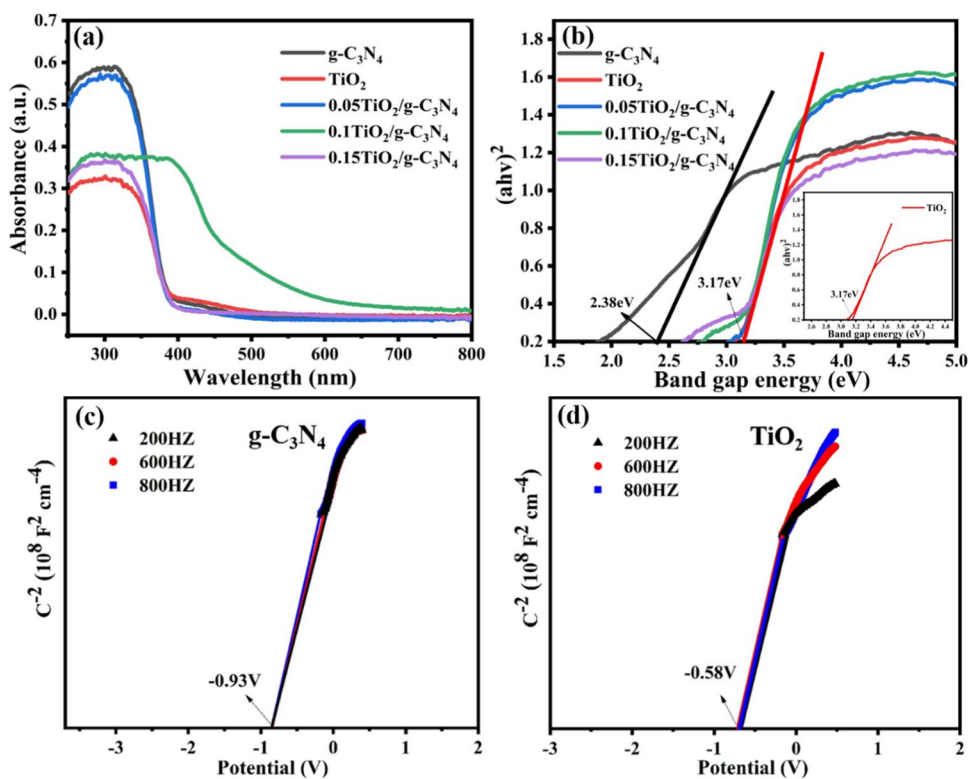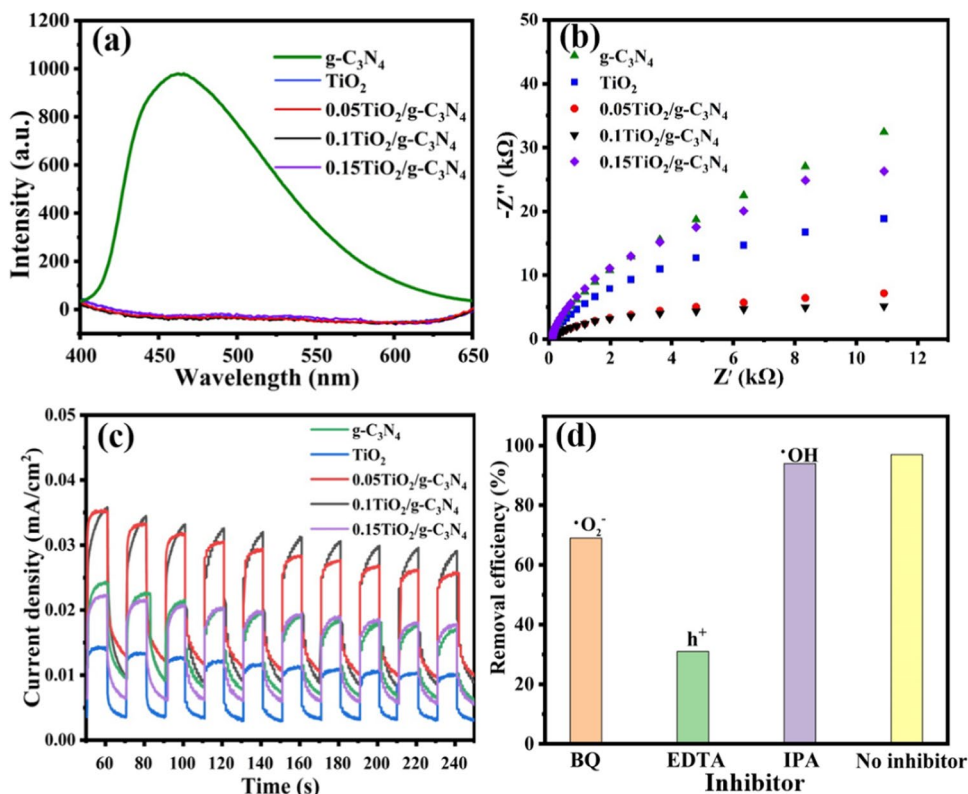

Fig. 5 **a** PL spectra, **b** EIS curves, and **c** transient photo-current response of different samples. **d** Effects of different scavengers on TC degradation

to pure g-C_3N_4. Nonetheless, photocurrent intensity of 0.15TiO_2/g-C_3N_4 was close to pure g-C_3N_4, signifying that excessive loading of TiO_2 could hinder the transfer and separation of carries due to its damaged heterojunction structure. And 0.1TiO_2/g-C_3N_4 had the highest photocurrent intensity in all samples, further proving the highest separation and migration rate of carriers attributed to the outstanding synergistic effect from applicable core–shell heterojunction, which was agreed with the result in Fig. 5b. The arc radius of EIS Nyquist plots in Fig. 5b reflected the surface reaction velocity (*Vr*) and interfacial charge transfer resistance (*Rc*) of the photocatalyst. Generally, the charge transfer resistance would be lower with smaller arc radius, which was more conductive to the charge move across the surface. Therefore, arc radius of *x*TiO_2/g-C_3N_4 were smaller than single g-C_3N_4 along with a faster charge transfer rate which clarified the rapid charge transfer of the composites owing to the construction of heterojunctions. Moreover, with raising TiO_2 amount, the arc radius of the composites gradually reduced then rapidly enlarged, demonstrating that TiO_2 amount had a vital impact on the charge transfer efficiency of *x*TiO_2/g-C_3N_4. Among them, 0.1TiO_2/g-C_3N_4 presented the smallest arc radius, indicating that 0.1TiO_2/g-C_3N_4 had the lowest *Rc* value and the fastest *Vr*. These above results demonstrated that 0.1TiO_2/g-C_3N_4 had the longest carrier lifetime and the fastest separation efficiency, leading to the best degradation ability of TC on account of the formation of an optimal heterojunction structure and acquisition of more active sites. In addition, in order to study the active radicals which played a major effect in the process of TC degradation, different inhibitors were added for experiments. In a word, the BQ, EDTA, and IPA were used as the scavengers to determine the effect of $\cdot O_2^-$, h^+, and $\cdot OH$ in the degradation process, respectively (Zhu et al. 2019). Figure 5d shows the removal efficiency of 0.1TiO_2/g-C_3N_4 distinctly decreased after the addition of BQ and EDTA, while the removal efficiency displayed a minor decline when adding IPA compared with the condition without scavengers, indicating the free radicals ($\cdot O_2^-$) and h^+ played crucial roles in photocatalytic process.
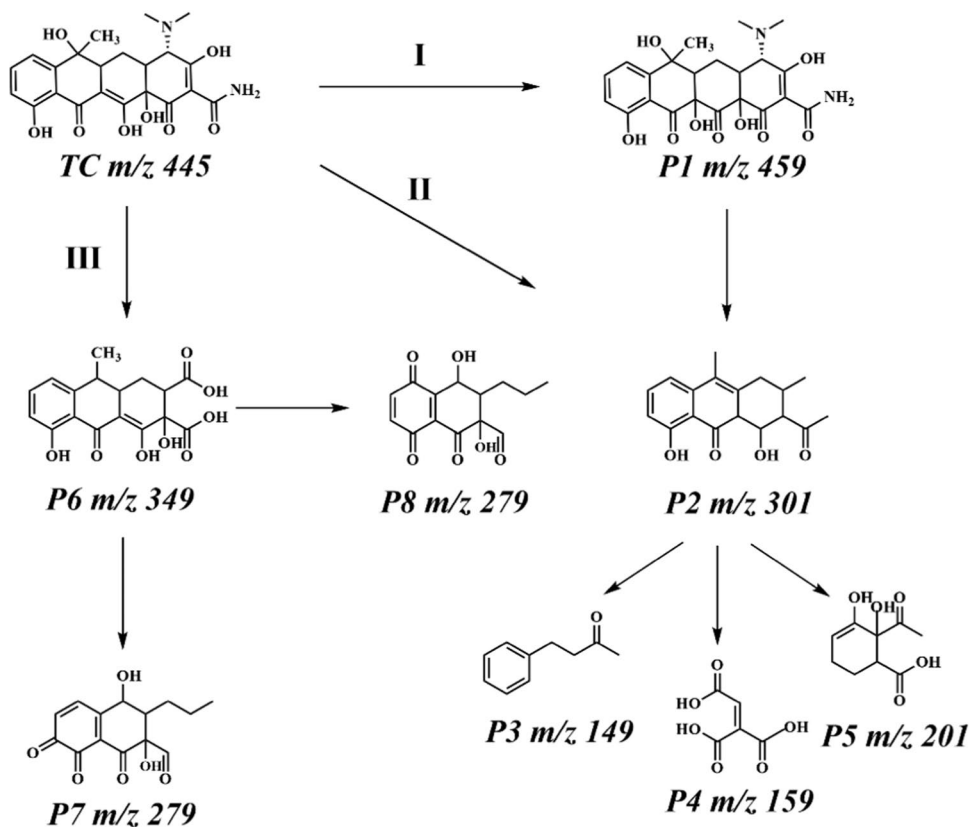
Fig. S5 presents the photocatalytic cyclic curves and removal efficiencies of 0.1TiO_2/g-C_3N_4 at the typical conditions. It could be seen that the sample maintained high photocatalytic degradation efficiency of about 99% after four cycles, which indicated that the sample had excellent cycle stability and photocorrosion resistance. It was expected that the hierarchical and coated composites had good application prospects in degrading antibiotics. Fig. S5(c) shows the XRD pattern before and after four times of photocatalysis. After cycles, no obvious changes were in spectrum and no diffraction peaks of other impurities were found which meant synthesized TiO_2/g-C_3N_4 composite had extremely high stability.

TRPL was used to analyze the average lifetime of the photogenerated carrier of sample in Fig. S6. The average lifetime of g-C_3N_4, TiO_2, and 0.1TiO_2/g-C_3N_4 were 5.26, 1.07, and 1.68 ns when the sample was excited at 337 nm and calculated by double exponential fitting. As a rule, the longer the material life meant, the lower the recombination rate of photogenerated carriers, and the lifetime of TiO_2 after loading g-C_3N_4 was significantly enhanced, thus corroborating the construction of heterojunction significantly accelerated the division and transfer of photoinduced carriers. The recombination of electron and hole was inhibited, and the photocatalytic activity was enhanced.
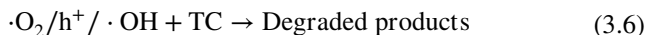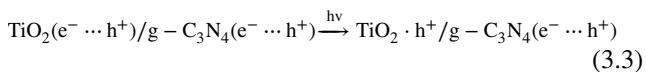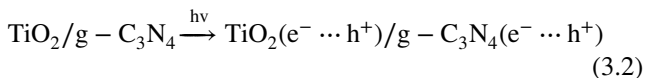
In order to clarify the degradation pathway and the intermediates molecules generated during the degradation process of TC, the degradation products were collected from reaction mixtures at different irradiation times by LC–MS test. In conformity with the LC–MS spectra (Fig. S7), the *m/z* values of major intermediates were 459,301, 349, 279, 201, 149, and 159, respectively. By analyzing LC–MS spectra (Fig. S7) and referring to earlier reports (Dong et al. 2018), the decomposition pathway of TC and molecular structure of intermediate during degradation were listed (Table S1). TC degradation by TiO_2/g-C_3N_4 had three main pathways (Fig. 6): First, for path I, TC (*m/z* = 445) was hydroxylated, then broken into P1 (*m/z* = 459). After the dehydroxylation reaction and deamination reaction, the c = c bonds formed P2 under $\cdot OH$ and $\cdot O_2^-$ attack (Gan et al. 2022). Alternatively, P2 (*m/z* = 301) could be obtained directly from path II by oxidation ring opening under the action of free radicals (Liu et al. 2020). Finally, the intermediates were broken down into smaller molecules (*m/z* = 149, 116, and 201). For path III, TC was attacked by $\cdot OH$ and carbon atom ring was cleaved to achieve intermediate P6 (*m/z* = 349) (Bai et al. 2019), and then, after decarboxylation reaction, P7 (*m/z* = 279) and P8 (*m/z* = 279) were obtained under attack of reactive radical (Guo et al. 2021).

Figure S8 and the formula (3.2)–(3.6) present the feasible diagrammatic drawing of direct Z-type photocatalytic mechanism to explain the elevation of photocatalytic capability for 0.1TiO_2/g-C_3N_4. First, TiO_2 along with g-C_3N_4 both generated photo-induced electron–hole pairs via light irradiation. The photocatalytic reactions of direct Z-type TiO_2/g-C_3N_4 composite were as followed. The CB of TiO_2 generated electrons which could move to the VB of g-C_3N_4 and combined with holes in the VB of g-C_3N_4, ensuring the CB of g-C_3N_4 had strong reducing action electrons and the VB of TiO_2 had high oxidation holes, which was identified as a direct Z-type charge divorce path. Concurrently, the CB of g-C_3N_4 could reduce O_2 to form $\cdot O_2^-$ with electrons in it, and then, free radical $\cdot O_2^-$ could strongly oxidize TC to obtain small molecule products (e.g., CO_2 and H_2O) because g-C_3N_4 had more negative CB potential than that of $O^2/\cdot O_2^-$ (−0.33 eV vs. NHE). As a result, the free radicals ($\cdot O_2^-$) and h^+ participated in the

Fig. 6 The degradation routes of TC in g-C$_3$N$_4$/TiO$_2$ system

oxidization reactions played the good roles in degrading TC. Thus, the VB of TiO$_2$ could directly oxidize TC by h^+ in it because the level of its VB was positive than the standard redox potential of OH$^-$/·OH (2.29 eV vs. NHE). However, the VB level of g-C$_3$N$_4$ was dissatisfied with the redox potential of OH$^-$/·OH, suggesting that it was impossible transfer h^+ from VB in TiO$_2$ to VB in g-C$_3$N$_4$ (Jiang et al. 2017), indicating that direct Z-type photocatalytic mechanism was viable. In Z-type pathway, the composite with good light absorption ability was excited to obtain amounts of photo-generated carries, and then, these carriers were effectively separated and transferred and the composite retained the excellent oxidation property to degrade TC, which were ascribed to the synergistic effect of core–shell TiO$_2$/g-C$_3$N$_4$ structure to form an optimized interface and abundant surface –active sites.

$$TiO_2/g - C_3N_4 \xrightarrow{hv} TiO_2(e^- \cdots h^+)/g - C_3N_4(e^- \cdots h^+) \quad (3.2)$$

$$TiO_2(e^- \cdots h^+)/g - C_3N_4(e^- \cdots h^+) \xrightarrow{hv} TiO_2 \cdot h^+/g - C_3N_4(e^- \cdots h^+) \quad (3.3)$$

$$e^- + O_2 \rightarrow \cdot O_2^- \quad (3.4)$$

$$h^+ + H_2O \rightarrow \cdot OH \quad (3.5)$$

$$\cdot O_2/h^+/ \cdot OH + TC \rightarrow Degraded\ products \quad (3.6)$$

Conclusions

Briefly, we successfully prepared the hierarchical g-C$_3$N$_4$/TiO$_2$ composites via template method followed by pyrolysis. The tight Z-type heterojunction was constructed via using TiO$_2$ as thick core and g-C$_3$N$_4$ as ultra-thin shell. The g-C$_3$N$_4$/TiO$_2$ composites had good ability to degrade TC under ultraviolet light (365 nm, 200–400 nm), especially in single-band 365 nm. During the degradation process, ·O$_2^-$ and h^+ played critical roles in improving TC degradation effect. Among these composites, 0.1TiO$_2$/g-C$_3$N$_4$ had the finest photocatalytic degradation capability, and degradation rate constant K was 0.049, which was about 49 and 23 times superior to single g-C$_3$N$_4$ and TiO$_2$, respectively. On account of construction of direct Z-type heterojunction with core–shell structure and favorable contact interface, 0.1 g-C$_3$N$_4$/TiO$_2$ has high separation and transfer rate of carriers, resulting in its excellent photocatalytic performance. The core–shell TiO$_2$/g-C$_3$N$_4$ Z-type photocatalyst shows the advantages of low cost, high activity, and superior stability, which can be expected for removing numerous refractory

pollutants from pharmaceutical wastewater, dye wastewater, and pesticide wastewater.

Data Availability The datasets used and/or analysed during the current study available from the corresponding author on request.

Declarations

Ethics approval Not applicable.

Consent to participate Not applicable.

Consent for publication The authors affirm that human research participants provided informed consent for publication of the images in Fig. 1 a, b, and c.

Competing interests The authors declare no competing interests.

References

Bai X, Wang Y, Li Y, Wang X (2019) Adsorption–photocatalytical remediation for series of tetracycline contaminants with BiOCl–CdS composite under simulated sunlight. J Taiwan Inst Chem Eng 104:94–105. https://doi.org/10.1016/j.jtice.2019.08.016

Chen C, Zhang J, Xiong X, Lin J, Yang S, Xi J, Kong Z (2022) A novel Z-type multidimensional $FeSe_2$/CuSe heterojunction photocatalyst with high photocatalytic and photoelectrochemical performance. Int J Hydrog Energy 47(67):28879–28893. https://doi.org/10.1016/j.ijhydene.2022.06.219

Dewil R, Mantzavinos D, Poulios I, Rodrigo MA (2017) New perspectives for advanced oxidation processes. J Environ Manage 195:93–99. https://doi.org/10.1016/j.jenvman.2017.04.010

Dong G, Huang L, Wu X, Wang C, Liu Y, Liu G, Wang L, Liu X, Xia H (2018) Effect and mechanism analysis of MnO_2 on permeable reactive barrier (PRB) system for the removal of tetracycline. Chemosphere 193:702–710. https://doi.org/10.1016/j.chemosphere.2017.11.085

Fan D, Guo C, Ma H, Zhao D, Li Y, Wu D, Wei Q (2016) Facile fabrication of an aptasensor for thrombin based on graphitic carbon nitride/TiO_2 with high visible-light photoelectrochemical activity. Biosens Bioelectron 75:116–122. https://doi.org/10.1016/j.bios.2015.08.029

Gan W, Fu X, Guo J, Zhang M, Li D, Ding C, Lu Y, Wang P, Sun Z (2022) Ag nanoparticles decorated 2D/2D TiO_2/g-C_3N_4 heterojunction for efficient removal of tetracycline hydrochloride:

synthesis, degradation pathways, and mechanism. Appl Surf Sci 606:154837. https://doi.org/10.1016/j.apsusc.2022.154837

Guo J, Jiang L, Liang J, Xu W, Yu H, Zhang J, Ye S, Xing W, Yuan X (2021) Photocatalytic degradation of tetracycline antibiotics using delafossite silver ferrite-based Z-scheme photocatalyst: pathways and mechanism insight. Chemosphere 270:128651. https://doi.org/10.1016/j.chemosphere.2020.128651

Hao J, Zhang S, Ren F, Wang Z, Lei J, Wang X, Cheng T, Li L (2017) Synthesis of TiO_2@g-C_3N_4 core-shell nanorod arrays with Z-scheme enhanced photocatalytic activity under visible light. J Colloid Interface Sci 508:419–425. https://doi.org/10.1016/j.jcis.2017.08.065

Hao H, Wang Z, Shi J, Li X, Lang X (2018) Improving the visible light photocatalytic aerobic oxidation of sulfides into sulfoxides on dye-sensitized TiO_2. ChemCatChem 10(20):4545–4554. https://doi.org/10.1002/cctc.201801304

Hunge YM, Yadav AA, Kang SW, Kim H (2021) Photocatalytic degradation of tetracycline antibiotics using hydrothermally synthesized two-dimensional molybdenum disulfide/titanium dioxide composites. J Colloid Interface Sci 606:454–463. https://doi.org/10.1016/j.jcis.2021.07.151

Jiang D, Xiao P, Shao L, Li D, Chen M (2017) RGO-promoted all-solid-state g-C_3N_4/$BiVO_4$ Z-scheme heterostructure with enhanced photocatalytic activity toward the degradation of antibiotics. Ind Eng Chem Res 56(31):8823–8832. https://doi.org/10.1021/acs.iecr.7b01840

Jiang G, Geng K, Wu Y, Han Y, Shen X (2018a) High photocatalytic performance of ruthenium complexes sensitizing g-C_3 N_4 /TiO_2 hybrid in visible light irradiation. Appl Catal B 227:366–375. https://doi.org/10.1016/j.apcatb.2018.01.034

Jiang X, Xing Q, Luo X, Li F, Zou J, Liu S, Li X, Wang X (2018b) Simultaneous photoreduction of Uranium(VI) and photooxidation of arsenic (III) in aqueous solution over g-C_3 N_4 /TiO_2 heterostructured catalysts under simulated sunlight irradiation. Appl Catal B 228:29–38. https://doi.org/10.1016/j.apcatb.2018.01.062

Jo WK, Natarajan TS (2015) Influence of TiO_2 morphology on the photocatalytic efficiency of direct Z-scheme g-C_3N_4/TiO_2 photocatalysts for isoniazid degradation. Chem Eng J 281:549–565. https://doi.org/10.1016/j.cej.2015.06.120

Kayal A, Mandal S (2022) Microbial degradation of antibiotic: future possibility of mitigating antibiotic pollution. Environ Monit Assess 194(9):639. https://doi.org/10.1007/s10661-022-10314-2

Kong L, Zhang X, Wang C, Xu J, Du X, Li L (2018) Ti^{3+} defect mediated g-C_3N_4/TiO_2 Z-scheme system for enhanced photocatalytic redox performance. Appl Surf Sci 448:188–296. https://doi.org/10.1016/j.apsusc.2018.04.011

Li J, Zhang M, Li X, Li Q, Yang J (2017) Effect of the calcination temperature on the visible light photocatalytic activity of direct contact Z-scheme g-C_3N_4-TiO_2 heterojunction. Appl Catal B 212:106–114. https://doi.org/10.1016/j.apcatb.2017.04.061

Li Y, Chang H, Wang Z, Shen Q, Liu X, Xue J, Jia H (2022) A 3D C@TiO_2 multishell nanoframe for simultaneous photothermal catalytic hydrogen generation and organic pollutant degradation. J Colloid Interface Sci 609:536–546. https://doi.org/10.1016/j.jcis.2021.11.052

Liu F, Nguyen TP, Wang Q, Massuyeau F, Dan Y, Jiang L (2019) Construction of Z-scheme g-C_3N_4/Ag/P3HT heterojunction for enhanced visible-light photocatalytic degradation of tetracycline (TC) and methyl orange (MO). Appl Surf Sci 496:143653. https://doi.org/10.1016/j.apsusc.2019.143653

Liu B, Sun Y, Zheng T, He X, Wang P, Wang J (2020) Wang Regeneration of carbon nanotube saturated with tetracycline by microwave-ultraviolet system: performance and degradation pathway. Chem Eng J 394:124752. https://doi.org/10.1016/j.cej.2020.124752

Maziarz W (2019) TiO$_2$/SnO$_2$ and TiO$_2$/CuO thin film nano-heterostructures as gas sensors. Appl Surf Sci 480:361–370. https://doi.org/10.1016/j.apsusc.2019.02.139

Meng A, Zhang L, Cheng B, Yu J (2019) Dual cocatalysts in TiO$_2$ photocatalysis. Adv Mater 31(30):1807660. https://doi.org/10.1002/adma.201807660

Milh H, Yu X, Cabooter D, Dewil R (2021) Degradation of ciprofloxacin using UV-based advanced removal processes: comparison of persulfate-based advanced oxidation and sulfite-based advanced reduction processes. Sci Total Environ 764:144510. https://doi.org/10.1016/j.scitotenv.2020.144510

Monga D, Basu S (2019) Enhanced photocatalytic degradation of industrial dye by g-C$_3$N$_4$/TiO$_2$ nanocomposite: role of shape of TiO$_2$. Adv Powder Technol 30(5):1089–1098. https://doi.org/10.1016/j.apt.2019.03.004

Pan J, Zhang Y, Guan Y, Yan Y, Tang H, Liu X, Wang M, Wei X (2022) Multifunctional Ni nanoparticles decorated SiC nanofibers/g-C$_3$N$_4$ nanosheets heterojunctions for drastically increased LED-light-driven hydrogen generation. Appl Surf Sci 579:152171. https://doi.org/10.1016/j.apsusc.2021.152171

Pan J, Guan Y, Zhang Y, Xu Z, Han S, Tang H, Yan X, Liu H, Lu Q (2023) Near-infrared-induced photothermal enhanced photocatalytic H$_2$ production for 3D/2D heterojunctions of snowflake-like CuS/g-C$_3$N$_4$ nanosheets. Inorg Chem 62(1):624–635. https://doi.org/10.1021/acs.inorgchem.2c04000

Perumal K, Shanavas S, Ahamad T, Karthigeyan A, Murugakoothan P (2023) Construction of Ag$_2$CO$_3$/BiOBr/CdS ternary composite photocatalyst with improved visible-light photocatalytic activity on tetracycline molecule degradation. J Environ Sci-China 125:47–60. https://doi.org/10.1016/j.jes.2021.10.021

Qiu J, Feng Y, Zhang X, Zhang X, Jia M, Yao J (2018) Facile stir-dried preparation of g-C$_3$N$_4$/TiO$_2$ homogeneous composites with enhanced photocatalytic activity. RSC Adv 7(18):10668–10674. https://doi.org/10.1039/c7ra00050b

Rehman ZU, Bilal M, Hou J, Butt FK, Ahmad J, Ali S, Hussain A (2022) Photocatalytic CO$_2$ reduction using TiO$_2$-based photocatalysts and TiO$_2$ Z-scheme heterojunction composites: a review. Molecules 27(7):2069. https://doi.org/10.3390/molecules27072069

Tang R, Gong D, Deng Y, Xiong S, Zheng F, Li L, Zhou Z, Su L, Zhao J (2021) π-π stacking derived from graphene-like biochar/g-C$_3$N$_4$ with tunable band structure for photocatalytic antibiotics degradation via peroxymonosulfate activation. J Hazard Mater 423:126944. https://doi.org/10.1016/j.jhazmat.2021.126944

Xu W, Lai S, Pillai SC, Chu W, Hu Y, Jiang X, Fu M, Wu X, Li F, Wang H (2020) Visible light photocatalytic degradation of tetracycline with porous Ag/graphite carbon nitride plasmonic composite: degradation pathways and mechanism. J Colloid Interface Sci 574:110–121. https://doi.org/10.1016/j.jcis.2020.04.038

Yu J, Wang S, Low J, Xiao W (2013) Enhanced photocatalytic performance of direct Z-scheme g-C$_3$N$_4$-TiO$_2$ photocatalysts for the decomposition of formaldehyde in air. Phys Chem Chem Phys 15(39):16883–16890. https://doi.org/10.1039/c3cp53131g

Yu H, Wang D, Zhao B, Lu Y, Wang X, Zhu S, Qin W, Huo M (2020) Enhanced photocatalytic degradation of tetracycline under visible light by using a ternary photocatalyst of Ag$_3$PO$_4$/AgBr/g-C$_3$N$_4$ with dual Z-scheme heterojunction. Sep Purif Technol 237:116365. https://doi.org/10.1016/j.seppur.2019.116365

Zhang B, He X, Yu C, Liu G, Ma D, Cui C, Yan Q, Zhang Y, Zhang G, Ma J, Xin Y (2022) Degradation of tetracycline hydrochloride by ultrafine TiO$_2$ nanoparticles modified g-C$_3$N$_4$ heterojunction photocatalyst: influencing factors, products and mechanism insight. Chin Chem Lett 33(3):1337–1342. https://doi.org/10.1016/j.cclet.2021.08.008

Zhu Q, Sun Y, Xu S, Li Y, Lin X, Qin Y (2019) Rational design of 3D/2D In$_2$O$_3$ nanocube/ZnIn$_2$S$_4$ nanosheet heterojunction photocatalyst with large-area "high-speed channels" for photocatalytic oxidation of 2,4-dichlorophenol under visible light. J Hazard Mater 382:121098. https://doi.org/10.1016/j.jhazmat.2019.121098

Zong H, Zhao T, Zhou G, Qian R, Feng T, Pan J (2019) Revisiting structural and photocatalytic properties of g-C$_3$N$_4$/TiO$_2$: is surface modification of TiO$_2$ by calcination with urea an effective route to "solar" photocatalyst? Catal Today 335:252–261. https://doi.org/10.1016/j.cattod.2018.12.015

Zuo G, Wang Y, Teo W, Xian Q, Zhao Y (2021) Direct Z-scheme TiO$_2$–ZnIn$_2$S$_4$ nanoflowers for cocatalyst-free photocatalytic water splitting. Appl Catal B 291:120126. https://doi.org/10.1016/j.apcatb.2021.120126